Radiological Physics and Technology (2019) 12:76–85
https://doi.org/10.1007/s12194-018-00494-3

Influence of field-of-view and section thickness of diagnostic imaging on thermal neutron flux estimation in dose-planning for boron neutron capture therapy

Hiroyuki Sato[1,2] · Takushi Takata[3] · Yoshinori Sakurai[3]

Received: 18 June 2018 / Revised: 10 December 2018 / Accepted: 11 December 2018 / Published online: 19 December 2018

Abstract
Radiation treatment planning for boron neutron capture therapy (BNCT) often uses computed tomography (CT) images reconstructed utilizing various section thickness and field-of-view (FOV) settings. Based on these images, a geometrical model is created by setting material regions manually over the pixel space defined in the treatment planning system. Thus, a setting difference of several pixels inevitably occurs in creation of the model. The influence of different section thicknesses and FOVs on thermal neutron flux estimations using the BNCT planning system was studied here. A virtual phantom was created with six FOV sizes on the planning system. The position of the irradiated side of the phantom surface was shifted by 1–10 pixels along the beam direction or in the opposite direction to simulate the material setting on different pixels in the geometric model. The effect of a one-pixel-difference setting on thermal neutron flux increased with increasing FOV size. Next, a cylindrical and a spherical phantom were scanned, and each CT image was reconstructed with six FOV sizes and seven section thicknesses. The flux changes for all conditions were compared, with an allowable error rate of ± 0.05, as in conventional X-ray radio therapy. The accuracy of neutron flux estimations was also evaluated by repeating the calculation procedures with CT scanning 5 or 10 times, and was found to be mostly within 0.03, except for the FOV-500 condition (0.074). These results suggested that a smaller FOV and section thickness with realistic conditions could improve evaluation accuracy of the thermal neutron flux for BNCT.

Keywords Boron neutron capture therapy · Epi-thermal neutron flux · Field-of-view · Section thickness · Thermal neutron flux · Treatment planning

1 Introduction

Boron neutron capture therapy (BNCT) is a particle therapy in which a compound containing boron-10 (^{10}B) is administered to a patient and allowed to accumulate in tumor cells. This is followed by irradiation of the diseased region with neutrons, causing a ^{10}B (n, α) ^{7}Li reaction in the cells containing the compound [1–3]. This reaction primarily involves thermal neutrons, and the path lengths of ^{4}He particles and ^{7}Li particles released are 8 μm and 5 μm, respectively, which is the size range of a typical cell, allowing selective tumor cell killing [4–6]. Neutrons entering the body are decelerated and diffused mainly by elastic scattering by hydrogen nuclei and undergo increasing attenuation at greater depths [7, 8]. Hydrogen density distribution is important for dose calculation in planning BNCT.

In a conventional radiotherapy planning system, dose is calculated using the relative electron density converted from computed tomography (CT) values [9, 10]. In the BNCT treatment planning system, using the Simulation Environment for Radiotherapy Applications (SERA), system-specific values such as hydrogen density are set manually to a certain pixel area according to anatomical structure [11–15]. Therefore, setting difference of several pixels in geometric model creation cannot be avoided as demonstrated in Fig. 1. Because pixel size (mm per pixel) escalates with increasing

✉ Yoshinori Sakurai
yosakura@rri.kyoto-u.ac.jp

[1] Graduate School of Engineering, Kyoto University, Kyoto, Japan

[2] Department of Radiology, Tottori University Hospital, Tottori, Japan

[3] Institute for Integrated Radiation and Nuclear Science, Kyoto University, Osaka, Japan

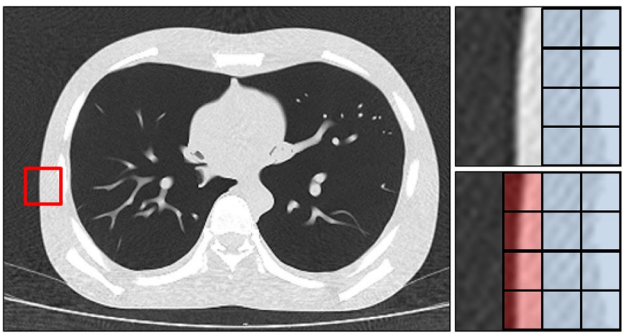

Fig. 1 An example of creating a geometric model for the chest is shown. The area enclosed by the red square in the left image is enlarged on the two right images. The upper and lower images on the right represent the same region. Blue and red squares indicate pixels including the chest wall set in the geometric model. Because the pixel setting in geometric model creation is performed manually, the upper and the lower pattern on right images are generated. As indicated by the red squares, different pixel settings may occur

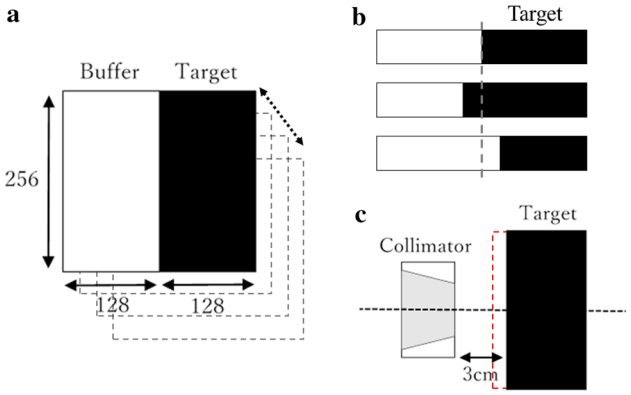

Fig. 2 Geometry of the target. **a** The setting of the target in a SERA model. The target area was assigned the physical density and composition of soft tissue. The buffer area, which is outside the calculation region, does not affect the calculation. The geometry was constructed by stacking 25 sections (dotted arrow) at 10-mm intervals, i.e., "pixel-0 geometry". **b** The upper panel shows "pixel-0 geometry", the middle panel shows an example of adding the pixels of the target, while the bottom panel shows an example of subtracting the pixels of the target. The dotted line shows the surface of "pixel-0 geometry". The left side is the irradiation side. **c** The geometry of irradiation for pixel-0 geometry. The distance from the collimator to the surface of the target is 3 cm. The red dotted line shows the case of adding the pixels of the target. The distance between the collimator and the surface of the target is small

FOV size, a setting difference of several pixels in geometric model creation may result in a large dose error. The treatment plan is sometimes created based on CT or magnetic resonance (MR) images acquired at referral hospitals, with different image reconstruction conditions for field-of-view (FOV) and different section thicknesses. These differences influence dose estimations in BNCT planning; however, this has not been studied in detail to date. There is no guideline for FOV and section thickness selection in current BNCT treatment planning.

In this study, we evaluated the influence of FOV size and section thickness on thermal neutron flux, which mostly affects the dose, for SERA. Our aim was to provide the optimal FOV size and section thickness for BNCT planning.

2 Materials and methods

2.1 Effect of pixel setting error

The dose calculation algorithm for SERA is based on a Monte Carlo method, and consists of seven modules. In the "SERA_MODEL" module, geometric models used for dose calculations are prepared by setting material regions manually over a 256×256 pixel area with the image section thickness. The voxel size for dose calculations is fixed at 10 mm^3 in the SERA module and is used for the practical application to the current clinical BNCT study. Use of a smaller voxel size is currently limited due to the realistic calculation time in a clinical context.

In this evaluation, from among a total square area of 256×256 pixels, the right half (128×256 pixels), was set as the target area, and the remaining half was set as the buffer area (Fig. 2a). The target area was assigned the physical density and composition of soft tissue. The buffer area, outside of the calculation region, does not affect the calculation. Because it is necessary to define material for all pixels in the reference image, the area outside the geometric model was defined as the buffer area. The geometry was constructed by stacking 25 sections at 10-mm intervals, i.e., "pixel-0 geometry" (Fig. 2a). The position of the irradiation side of the virtual phantom was shifted by 1–10 pixels along the beam directions, or the opposite direction, to simulate the different settings of pixels in the geometric model; these are defined as pixel setting errors and are shown in Fig. 2b. In pixel + 1 to + 10 geometries the irradiated side of the target was shifted by 1–10 pixels in the direction opposite to the beam direction, as shown in the middle of Fig. 2b, while in pixel − 1 to − 10 geometries, the side of the target was shifted along the beam direction, as shown in the lower part of Fig. 2b. All geometries were prepared for FOVs of 200, 250, 300, 350, 400, and 500 mm (Table 1). As shown in Fig. 2c, the beam axis was set to pass perpendicularly through the center of the target. The distance between collimator surface and target surface at pixel-0 geometry was set at 3 cm. This distance was decreased as the number of added pixels increased, and increased as the number of subtracted pixels increased. Source data were obtained from the standard thermal neutron irradiation mode of the Heavy Water Neutron Irradiation Facility installed in the Kyoto University Research Reactor (KUR). The collimator aperture was 12×12 cm, and irradiation time was assumed to be 60 min. The neutron flux

Table 1 The pixel size of each field-of-view (FOV)

FOV(mm)	200	250	300	350	400	500
Pixel size (mm per pixel)	0.78	0.98	1.17	1.37	1.56	1.95

at depths of 0, 2, and 5 cm from the phantom surface along the beam axis, which are important in clinical treatment, were evaluated. For the deviation of thermal neutron flux at each depth, the error rate (Eq. 1) was evaluated on the reference for pixel-0 geometry by the following equation:

$$\varepsilon = \frac{N_{\text{various pixels}} - N_{\text{pixel 0}}}{N_{\text{pixel 0}}}, \tag{1}$$

where $N_{\text{various pixels}}$ is the thermal neutron flux at each pixel setting error, and $N_{\text{pixel 0}}$ is the thermal neutron flux for pixel-0 geometry. Currently in BNCT, epi-thermal neutron irradiation is performed to improve thermal neutron flux distribution in the deeper regions. Hydrogen atoms in the body cause epi-thermal neutrons to lose energy and to change into thermal neutrons. Therefore, changes in the epi-thermal neutron flux influence the thermal neutron flux distribution in the body. The epi-thermal neutron flux was evaluated using the same methodology as that used for thermal neutron flux.

2.2 Effect of FOV

The effect of FOV on dose was evaluated using actual CT images of the phantom. The Tottori University Hospitals' 64-slice multi-detector CT scanner (Aquilion 64, Canon Medical Systems, Otawara, Japan) was used with the following imaging parameters: 120 kV tube voltage, 300 mA tube current, 1 s rotation time, and 1-mm section thickness, for 200, 250, 300, 350, 400, and 500-mm FOVs. To exclude the influence of other factors, such as shape, and to evaluate only the influence of a pixel-setting difference in geometric model creation, a simple cylindrical phantom (Japan Medical Service, Osaka, Japan), 16 cm in diameter and 15 cm in height, was used. As shown in Fig. 3, the beam axis was set to pass perpendicularly through the midpoint of the long axis of the phantom. The distance between the collimator surface and phantom surface was set at 2 cm. The neutron flux at depths of 0, 2, 5, and 8 cm from the phantom surface, along the beam axis, was evaluated. For determining the thermal neutron flux at each depth, an error rate based on FOV-250, which is typically used in head imaging, was evaluated using Eq. 2:

$$\varepsilon = \frac{N_{\text{each FOV}} - N_{\text{FOV 250}}}{N_{\text{FOV 250}}}, \tag{2}$$

where $N_{\text{each FOV}}$ is the thermal neutron flux for each FOV and $N_{\text{FOV 250}}$ is the thermal neutron flux at FOV-250. CT scanning of the phantom was repeated 10 times and the

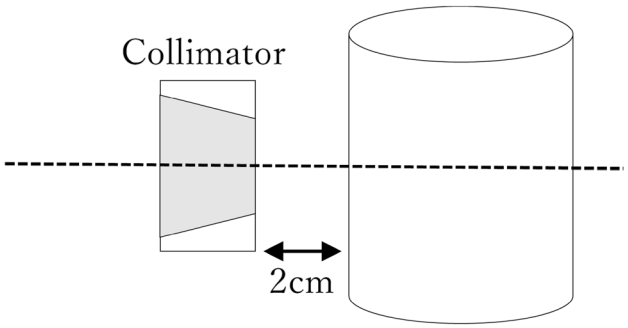

Fig. 3 The geometry of irradiation under computed tomography showing the effect of field-of-view (FOV). The distance from the collimator to the surface of the target is 2 cm. The dotted line shows the central axis of the beam

calculations were performed for each CT image in order to estimate calculation accuracy. The allowable value of the error rate was ±0.05, as is used in X-ray therapy. In order to evaluate the influence of calculation accuracy, the coefficient of variation (CV) of thermal neutron flux under each condition was calculated using the equation below:

$$\text{CV} = \frac{\text{Standard deviation}}{\text{Average value}}. \tag{3}$$

2.3 Effect of section thickness

The influence of section thickness on dose was evaluated using the same CT apparatus. FOV was set to 250 mm and the following seven values of section thickness were used: 1, 2, 3, 5, 7, 8, and 10 mm. A spherical phantom (3D Digital Image Phantom, Kyoto Kagaku, Kyoto, Japan) of 20-cm diameter was used to simulate a brain to be irradiated by BNCT from various angles. The geometrical center of the phantom was placed at the center of the FOV in the CT scanner and the images were reconstructed such that the phantom center was positioned at one-half of the section thickness for the middle slice. The distance between the collimator surface and the phantom surface was set at 1 cm, and the beam axis was set to pass through the phantom center (Fig. 4a). The neutron flux at depths of 0, 2, 5, and 8 cm from the phantom surface along the beam axis were evaluated. For thermal neutron flux at each depth, the error rate, based on 1-mm-section thickness, was evaluated using Eq. 4:

$$\varepsilon = \frac{N_{\text{each section thickness}} - N_{\text{1 mm thickness}}}{N_{\text{1 mm thickness}}}, \tag{4}$$

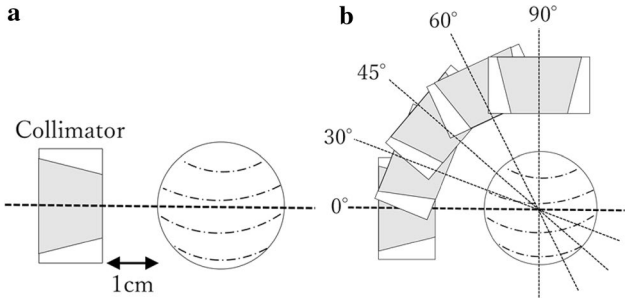

Fig. 4 The geometry for the section thickness. **a** The geometry of irradiation under computed tomography. The distance from the collimator to the surface of the target is 1 cm. **b** The geometry of irradiation at each irradiation angle. The dotted line shows an irradiation angle of 0°, where the irradiation direction is parallel to the section plane

where $N_{\text{each section thickness}}$ is the thermal neutron flux for each section thickness and $N_{1\text{ mm thickness}}$ is the thermal neutron flux at 1-mm-section thickness. These procedures from CT imaging, were repeated five times. As in Sect. 2.2, the allowable value for the error rate was ± 0.05. In order to evaluate the influence of calculation accuracy, the CV of thermal neutron flux under each condition was calculated (Eq. 3). In addition, the correlation between irradiation direction and section direction was evaluated. The irradiation angle was defined as 0° for the direction parallel to the section plane, and set at 30°, 45°, 60°, and 90° in the evaluation (Fig. 4b). The error rate based on 1-mm-section thickness was evaluated at each irradiation angle using Eq. 4. The evaluation method was the same as described above.

3 Results

3.1 Effect of pixel setting error

As an example, the penetrating depth distribution of thermal neutron flux in the pixel-0 geometry for an image condition with a FOV of 250 is shown in Fig. 5a. The neutron flux at depths of 0, 2, and 5 cm from the phantom surface, along the beam axis, were evaluated. The relationship between errors of pixel setting and the error ratio of thermal neutron flux at a 0-cm depth is shown in Fig. 5b. Periodic undulation was observed at FOVs of 300, 350, 400, and 500 mm. Table 2 shows the pixel setting errors and corresponding actual size (pixel size × pixel setting error) at the minimum error rate of the first cycle for each FOV condition. The periodic behavior of the error rate was confirmed for neutron flux at a depth of 0 cm. All pixel size values were found to be close to 10 mm of the calculation grid size. Periodicity was not observed at FOV-200 and FOV-250 in the pixel setting error range in this study, but showed the same tendency as that at other FOV. Data showed that the thermal neutron flux changed,

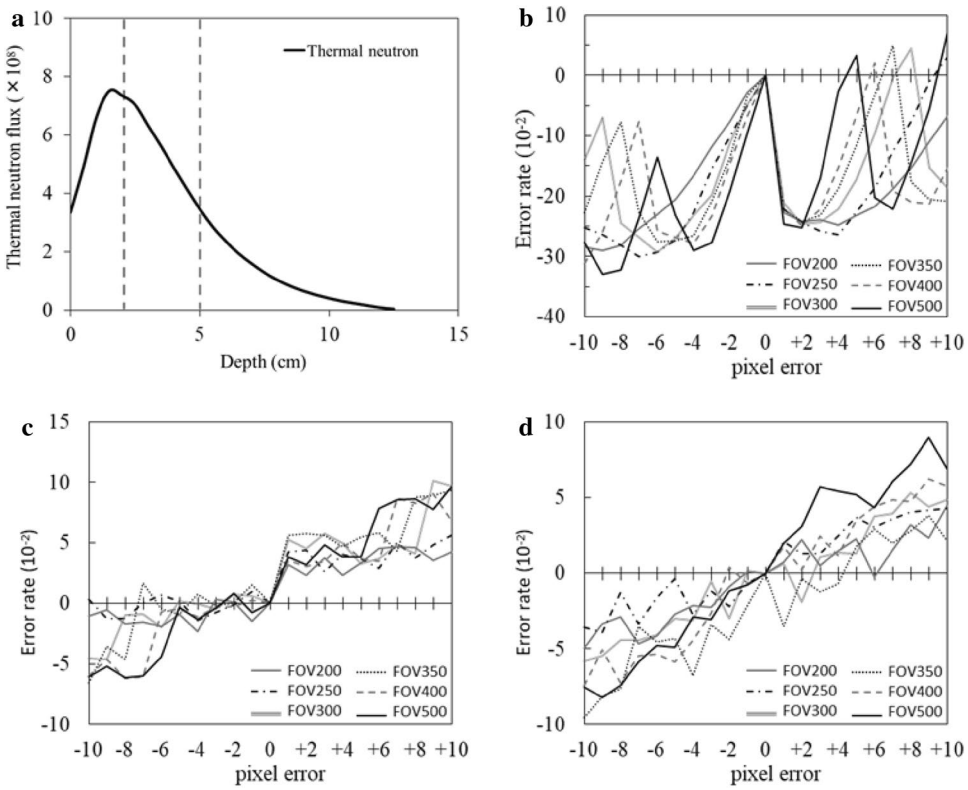

Fig. 5 The error rate of thermal neutron flux at each depth for pixel setting error. **a** As an example, the penetration depth distribution of thermal neutron flux in the pixel-0 geometry for an image condition with a FOV-250 is shown. The dotted lines show the depths of 0, 2, and 5 cm. **b** 0-cm depth. **c** 2-cm depth. **d** 5-cm depth

Table 2 The pixel setting error and corresponding actual size (pixel size × pixel setting error) at the minimum error rate of the first cycle for each field-of-view (FOV) condition

	FOV (mm)											
	300			350			400			500		
Pixel setting error	−9	0	+8	−8	0	+7	−7	0	+6	−6	0	+5
Actual size (mm)	−10.53	0	+9.36	−10.9	0	+9.59	−10.92	0	+9.36	−11.7	0	+9.75

The pixel setting error and the actual size at the peak within the period of the error rate in the FOV in which the periodicity was confirmed at a depth of 0 cm are shown

even for smaller pixel errors, as the FOV size increased. The results at 2-cm depth are shown in Fig. 5c. Stepwise periodicity was observed in the change in error rate. The error rate changed markedly in the same period as at 0-cm depth. The results at a depth of 5 cm are shown in Fig. 5d. The error rate increased with increasing pixel setting error. By fitting error rates with a first-order polynomial function, inclination coefficients were estimated to be 0.0041, 0.0043, 0.0055, 0.006, 0.0071, and 0.088 for FOV-200, -250, -300, -350, -400, and -500 mm, respectively, showing that the inclination became larger as the size of the FOV increased.

Because a change in epi-thermal neutron flux greatly influences thermal neutron flux, epi-thermal neutron flux was also evaluated using the same method as for thermal neutron flux. As an example, the penetration depth distribution of the epi-thermal neutron flux in the pixel-0 geometry for the FOV-250 image condition is shown in Fig. 6a. The relationship between pixel setting error and the error ratio of epi-thermal neutron flux at depths of 0, 2, and 5 cm is shown in Fig. 6b, c, d. At a depth of 0 cm, the periodic dependence of error rates was observed at FOVs of 300, 350, 400, and 500 mm, similar to that of thermal neutron flux. Error rates were about half of that for thermal neutron flux. At a depth of 2 cm, no stepwise periodicity, such as that in thermal neutron flux, was observed, but the error rate increased as the pixel setting error became larger. By fitting the error rates with a first-order polynomial function, inclination coefficients were estimated to be 0.0025, 0.0021, 0.0045, 0.0046, 0.0049, and 0.0056 for FOV-200, -250, -300, -350, -400, and -500 mm, respectively; thus, the inclination became larger as the size of the FOV increased. At a depth of 5 cm, no change in the error rate due to pixel setting error could be confirmed. However, the error rates were larger than those seen with thermal neutron flux.

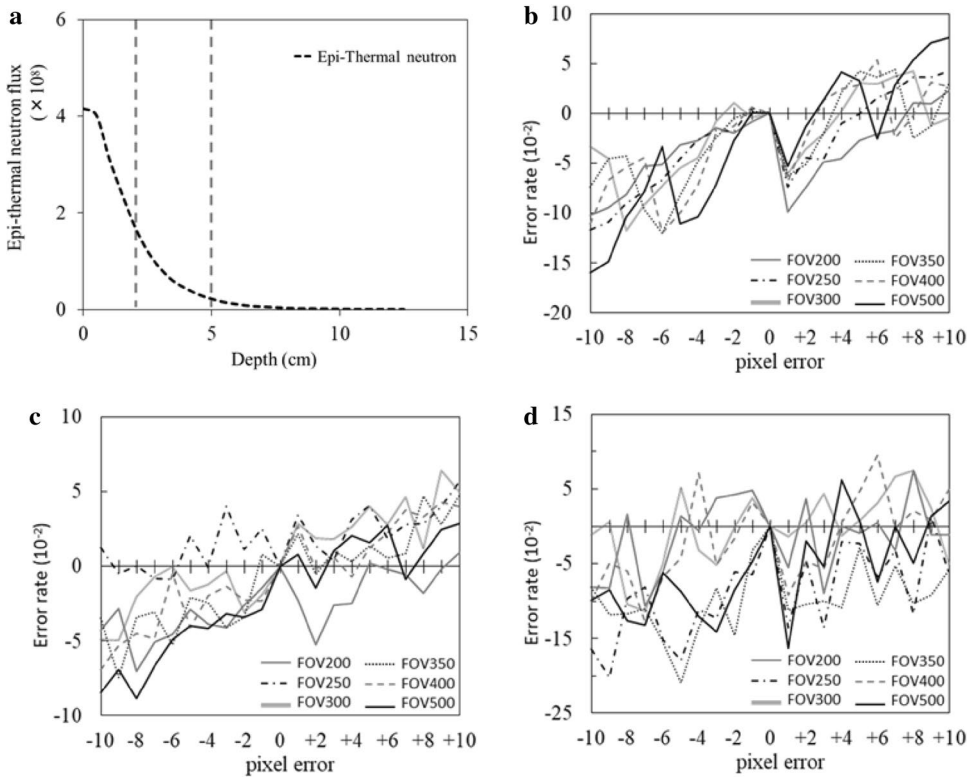

Fig. 6 The error rate of epi-thermal neutron flux at each depth for pixel setting error. **a** As an example, the penetration depth distribution of the epi-thermal neutron flux in the pixel-0 geometry for the image condition with a FOV-250 is shown. The dotted line shows the depths of 0, 2, and 5 cm. **b** 0-cm depth. **c** 2-cm depth. **d** 5-cm depth

3.2 Effect of FOV

The influence of FOV was evaluated using CT images of the cylindrical phantom. Figure 7 shows the error rate of thermal neutron flux at different depths for each FOV condition. The error rate was obtained by averaging data from 10 trials. No effect of FOV was observed at any depth. The neutron flux at 0-cm depth for FOV-300 deviated the most from the flux for FOV-250, but the corresponding error rate remained within the allowable error of ±0.05. Table 3 shows CV values obtained with Eq. 3 with 10 trials of neutron flux calculations for each FOV condition at different depths. A large CV was found for FOV-500 at a 0-cm depth. No difference in CV was confirmed under other conditions.

3.3 Effect of section thickness

The influence of section thickness was evaluated using CT images of the spherical phantom. Figure 8 shows the error rate of thermal neutron flux at different depths for each section thickness, with an irradiation angle of 0°. Error rates were obtained by averaging the data of five trials. No effects of section thickness were observed at depths of 0, 2, and 5 cm. The error rate at the depth of 8 cm became larger as the section thickness increased. The neutron flux with a section thickness of 8 mm at a depth of 0 cm deviated the most from the flux for a 1-mm thickness at the same depth, and the corresponding error rate was −0.06, which exceeded the allowable value of ±0.05 used for X-ray therapy. Table 4 shows CV values obtained by Eq. 3 with five trials of neutron flux calculations for each section thickness condition, at different depths. There was no correlation between CV and section thickness at an irradiation angle of 0°.

The influence of the relationship between section direction and irradiation direction was evaluated. Figure 9 shows the error rate of the thermal neutron flux irradiated from various angles at each depth and with each section thickness. At a depth of 0 cm (Fig. 9a), the neutron flux at all angles with larger section thicknesses showed a deviation larger than ±0.05 from a flux with 1-mm section thickness. The error rates at an angle of 45° were larger than those observed at other angles. The error rate at an irradiation angle of 30° exceeded the allowable value of ±0.05 only for a section thickness of 8 mm, at a 2-cm depth. Similarly, the error rates at an irradiation angle of 45° exceeded the allowable value for section thicknesses of 8 and 10 mm, at both 5-cm and

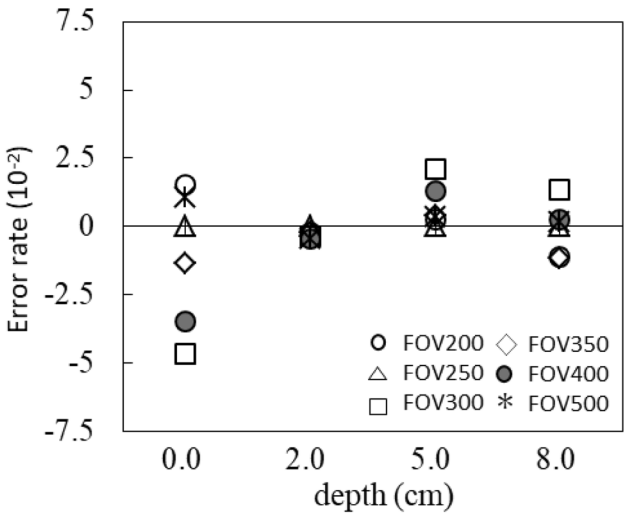

Fig. 7 The error rate of thermal neutron flux at different depths for each FOV condition. The error rate (Eq. 2) based on FOV-250, which is typically used in head imaging, was evaluated

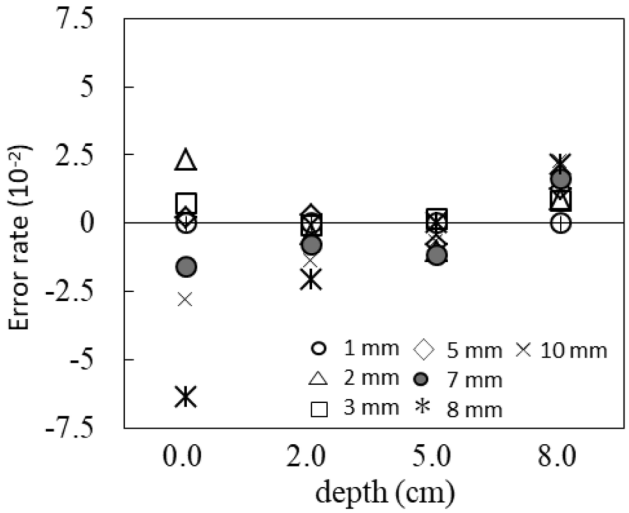

Fig. 8 The error rate of thermal neutron flux at different depths for each section thickness with an irradiation angle of 0°. The error rate (Eq. 4), based on 1-mm-section thickness, was evaluated

Table 3 Coefficient of variance (CV) values obtained by Eq. 3 for 10 trials of thermal neutron flux calculations for each field-of-view (FOV) condition at different depths

Depth (cm)	FOV (mm)					
	200	250	300	350	400	500
0	0.01074	0.01225	0.01243	0.00944	0.01674	0.07406
2	0.00588	0.00794	0.00912	0.01086	0.00537	0.00735
5	0.01060	0.00989	0.00925	0.01448	0.00809	0.02125
8	0.02108	0.02348	0.01482	0.01918	0.01391	0.02179

Table 4 Coefficient of variance values obtained by Eq. 3 with the calculations of five trials for each section thickness and irradiation angle

Irradiation angle (°)	Section thickness (mm)						
	1	2	3	5	7	8	10
Depth 0 cm							
0	0.0059	0.0143	0.0082	0.0095	0.0131	0.0158	0.0072
30	0.0121	0.0276	0.0153	0.0088	0.0174	0.0107	0.0061
45	0.0104	0.0253	0.0157	0.0106	0.0089	0.0119	0.0091
60	0.0114	0.0230	0.0103	0.0070	0.0094	0.0096	0.0115
90	0.0068	0.0148	0.0152	0.0031	0.0109	0.0070	0.0108
Depth 2 cm							
0	0.0087	0.0098	0.0065	0.0065	0.0101	0.0050	0.0098
30	0.0091	0.0154	0.0062	0.0061	0.0077	0.0026	0.0117
45	0.0087	0.0094	0.0084	0.0072	0.0030	0.0070	0.0100
60	0.0111	0.0066	0.0062	0.0119	0.0056	0.0067	0.0060
90	0.0047	0.0069	0.0049	0.0075	0.0073	0.0048	0.0122
Depth 5 cm							
0	0.0083	0.0113	0.0149	0.0064	0.0118	0.0142	0.0103
30	0.0168	0.0129	0.0109	0.0097	0.0117	0.0124	0.0068
45	0.0050	0.0143	0.0081	0.0084	0.0107	0.0105	0.0137
60	0.0184	0.0229	0.0141	0.0103	0.0095	0.0083	0.0147
90	0.0096	0.0328	0.0091	0.0036	0.0081	0.0073	0.0089
Depth 8 cm							
0	0.0093	0.0278	0.0159	0.0139	0.0060	0.0146	0.0162
30	0.0099	0.0187	0.0043	0.0048	0.0115	0.0208	0.0158
45	0.0142	0.0101	0.0128	0.0182	0.0227	0.0163	0.0109
60	0.0175	0.0337	0.0073	0.0108	0.0071	0.0184	0.0118
90	0.0079	0.0355	0.0129	0.0166	0.0102	0.0126	0.0112

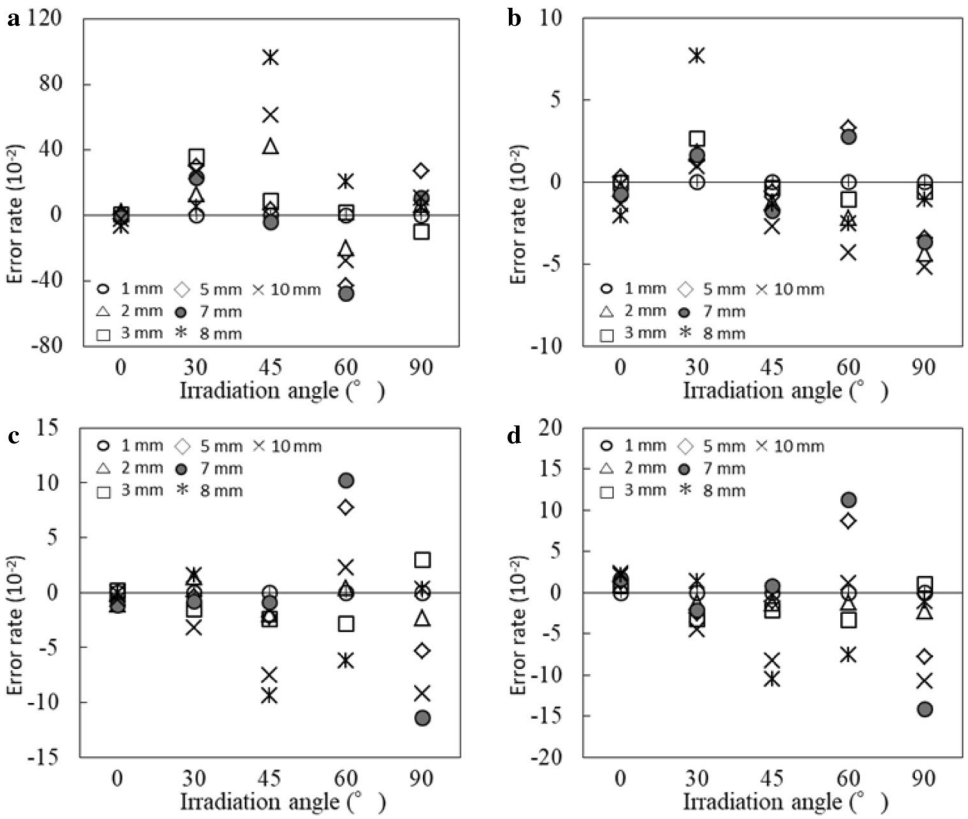

Fig. 9 The error rate of the thermal neutron flux irradiated from various angles at each depth and with each section thickness. **a** 0-cm depth. **b** 2-cm depth. **c** 5-cm depth. **d** 8-cm depth

8-cm depths. The error rates at an irradiation angle of 60° exceeded the allowable value in section thicknesses of 5, 7, and 8 mm at a 5-cm depth, and in section thicknesses of 5, 7, and 8 mm at an 8-cm depth. The error rates at an irradiation angle of 90° exceeded the allowable value for a section thickness of 10 mm at a 2-cm depth, in section thicknesses of 5, 7, and 10 mm at a 5-cm depth, and in section thicknesses of 5, 7 and 10 mm at an 8-cm depth. Table 4 shows the CV values obtained using Eq. 3 with calculations of five trials for each section thickness and irradiation angle. No correlation was found between section thickness and CV at any irradiation angle.

4 Discussion

Periodic dependence of the thermal neutron flux deviation due to the pixel setting error was found at shallow depths (0 cm and 2 cm, as shown in Fig. 5a, b). Wave-form dependence on error rates was observed at a 0-cm depth. In any FOV, the actual size converted from the pixel value was about 10 mm. It is likely that this periodicity resulted from the calculated voxel of 10 mm in SERA. In particular, at a depth of 0 mm, i.e., on the surface, the influence of pixel setting error was greater, because the buffer region and target region are present in one voxel, and parameters such as physical density and material density, etc., are averaged. This is one of the reasons for the rapid change in thermal neutron flux at near-surface depths [7]. Periodicity was not observed at a depth of 5 cm. The influence of several pixel setting errors becomes smaller at this depth, because changes in thermal neutron flux at this depth occur more slowly than at other depths. This implies that calculation accuracy was improved as the calculation grid size became smaller. However, the calculation grid size in SERA is a fixed value and cannot be changed. Kumada et al. suggested a planning system in which the calculation grid size can be changed. However, the influence of region setting differences in the geometric model has not been evaluated [8]. Our results confirmed that the influence of the setting error for one pixel was positively correlated with increases in FOV. Therefore, the FOV should be as small as possible in order to reduce the influence of the pixel setting error. In BNCT treatment planning at the Institute for Integrated Radiation and Nuclear Science, Kyoto University (KURNS), the prescribed dose is usually determined based on a peak dose (at a depth of almost 2 cm) or the surface dose (at a skin; i.e., a depth of 0 cm) for normal tissue [16–18]. The contribution of thermal neutrons to the dose is almost 70% at the peak dose and almost 55% at the surface dose. As shown in Sect. 3.1, a setting error of one pixel in thermal neutron flux is almost 5% at a depth of 2 cm and almost 25% at the surface. Therefore, an error rate of almost 3.5% for the peak dose and of almost 14% for the surface dose due to thermal neutrons should be considered when calculating the prescribed dose in treatment planning.

In the epi-thermal neutron flux, periodicity was observed only at a depth of 0 cm (Fig. 6). At depths of 2 cm and 5 cm, the error rates of the epi-thermal neutron flux were greater than those of the thermal neutron flux. This is because the gradient of the depth flux distribution of the epi-thermal neutron flux is steeper than that of thermal neutron flux. As shown in Figs. 5a and 6a, the distribution gradient of the epi-thermal neutron flux is steeper than that of the thermal neutron flux at depths of 2 and 5 cm. Therefore, the influence of a one-pixel difference is larger and the error ratio is greater for the epi-thermal neutron flux.

When evaluating the influence of FOV using CT images of the cylindrical phantom, error rates obtained from the mean of 10 trials were within ± 0.05 at any FOV (Fig. 7). However, the CV for FOV-500 at a 0-cm depth was greater than for other conditions. For FOV-500, calculation accuracy was noted to deteriorate. This emphasizes the necessity of selecting the smallest FOV possible, because calculation accuracy deteriorates when the FOV size is excessively large with respect to the subject diameter.

We evaluated the influence of different section thicknesses in CT images on the thermal neutron flux estimation, as compared to the flux of irradiation parallel to the section plane, using a spherical phantom. The error rate was -0.064 for a section thickness of 8 mm, at a depth of 0 cm; at other depths, the error rate did not exceed ± 0.05 (Fig. 8). The error rate at a section thickness of 10 mm was within the acceptable value, but it exceeded the acceptable value at a section thickness of 8 mm. Therefore, we recommend a section thickness less than 8 mm. However, section thickness had no apparent influence on CV. For the CV, this suggests that the difference in section thickness does not influence the accuracy of pixel setting in the slice plane, because the FOV used in this study was 250 mm. For the error rate, we consider that a geometric model in the slice thickness direction changes, particularly in a larger slice thickness, increasing the error rate.

In terms of the influence of section thickness on the irradiation angle, the magnitude of error rates exceeded the acceptable error of ± 0.05 at all angles at a depth of 0 cm (Fig. 9). In Particular, the error rate at an irradiation angle of 45° with a section thickness of 8 mm was 0.96. At a large angle of irradiation for the section plane, the error rate of the thermal neutron flux is considered to be larger, since the beam axis passes through multiple sections, and the influence of the pixel setting error from multiple sections is magnified. In addition, as shown in Fig. 9b, c, d, error rates exceeding the acceptable error of ± 0.05 at greater depths were also found at irradiation angles of 30° and 45°, for the section thicknesses of 8 and 10 mm, and at

the angles of 60° and 90°, for the thicknesses of 5–10 mm. Therefore, based on these data sets, we recommend that the neutron flux at an irradiation angle smaller than 45° should be estimated with a section thickness less than 8 mm, while at a larger angle, a thickness less than 5 mm should be used. In particular, in cases where there are numerous options for the irradiation angle, such as brain-tumor BNCT, the section thickness should be as small as possible. As shown in Table 4, there was no correlation between section thickness and CV at any irradiation angle. As with the influence of section thickness at the irradiation angle 0°, for the CV, this suggests that the difference in section thickness does not influence the accuracy of pixel setting in the slice plane, because the FOV used in this study was 250 mm. For the error rate, we consider that a geometric model in the slice thickness direction changes, particularly in a larger slice thickness, increasing the error rate. The error rate at irradiation angles of 30°–90° deteriorated greatly as compared with that at an irradiation angle of 0°, where the incident beam is parallel to the section plane. We consider that the beam is complicatedly incident to the calculation voxel, particularly at a larger irradiation angle, increasing the error rate.

5 Conclusions

In the BNCT treatment planning system, using "SERA", the influence of FOV and section thickness on thermal neutron flux was evaluated. Error was reduced and evaluation accuracy was improved by minimizing FOV and section thickness, and smaller section thickness was required when the irradiation angle of the section plane increased.

In addition, the influence of pixel setting error on thermal neutron flux was evaluated. Consequently, the periodicity of the error rate change was confirmed at a shallow depth. For software using relatively large calculation voxels, such as SERA, it is assumed that similar periodicity occurs. When using SERA, it is necessary to consider a maximum error rate of thermal neutron flux of almost 5% and 25% when determining the prescription peak dose (at a depth of 2 cm) and surface dose, respectively. Since the density distribution of hydrogen nuclei is manually determined through SERA, it is difficult to reduce these errors. Therefore, it is necessary to devise a method by which the dose can be calculated using the signal values from imaging data, similar to the process used when planning conventional X-ray therapy.

Currently, some BNCT treatment planning systems are under development. Therefore, further study is required to confirm the effect of FOV and section thickness on dose evaluation.

Compliance with ethical standards

Conflict of interest The authors declare that they have no conflicts of interest.

Research involving human participants and animals This article does not contain any studies with human participants performed. This article does not contain any studies with animals performed.

Informed consent Informed consent for this study was not required because no research involving human participants was undertaken by any of the authors.

References

1. Kruger PG. Some biological effects of nuclear disintegration products on neoplastic tissue. Proc Natl Acad Sci USA. 1940;26:181–92.
2. Gahbauer R, Gupta N, Blue T, Goodman J, Grecula J, Soloway AH, Wambersie A. BNCT: status and dosimetry requirements. Radiat Prot Dosim. 1997;70:547–54.
3. Barth RF, Coderre JA, Vicente MG, Blue TE. Boron neutron capture therapy of cancer: current status and future prospects. Clin Cancer Res. 2005;11:3987–4002.
4. Coderre JA, Morris GM. The radiation biology of boron neutron capture therapy. Radiat Res. 1999;151:1–18.
5. White SM, Held KD, Palmer MR, Yanch JC. Biological dosimetry for epithermal neutron beams. Radiat Res. 2001;155:778–84.
6. Rassow J, Pöller F, Steinberg F, Meissner P. Physical and tumor biological aspects and calculation model of dosage in boron neutron capture therapy (BNCT). Strahlenther Onkol. 1993;169:7–17.
7. Matsumoto T. Transport calculations of the influence of physical factors on depth-dose distributions in boron neutron capture therapy. Phys Med Biol. 1990;35:971–8.
8. Kumada H, Yamamoto K, Yamamoto T, Nakai K, Nakagawa Y, Kageji T, Matsumura A. Improvement of dose calculation accuracy for BNCT dosimetry by the multi-voxel method in JCDS. Appl Radiat Isot. 2004;61:1045–50.
9. Constantinou C, Harrington J, DeWerd L. An electron density calibration phantom for CT-based treatment planning computers. Med Phys. 1992;19:325–7.
10. Tsukihara M, Noto Y, Sasamoto R, Hayakawa T, Saito M. Initial implementation of the conversion from the energy-subtracted CT number to electron density in tissue inhomogeneity corrections: an anthropomorphic phantom study of radiotherapy treatment planning. Med Phys. 2015;42:1378–88.
11. Wessol DE, et al. SERA: simulation environment for radiotherapy applications user's manual version 1C0. INEEL/EXT-02-00698 (2002).
12. Kumada H, Yamamoto K, Matsumura A, Yamamoto T, Nakagawa Y, Nakai K, Kageji T. Verification of the computational dosimetry system in JAERI (JCDS) for boron neutron capture therapy. Phys Med Biol. 2004;49:3353–65.
13. Li HS, Liu YW, Lee CY, Lin TY, Hsu FY. Verification of the accuracy of BNCT treatment planning system THORplan. Appl Radiat Isot. 2009;67:122–5.
14. Zamenhof R, Redmond E, Solares G, Katz D, Riley K, Kiger S, Harling O. Monte Carlo-based treatment planning for boron neutron capture therapy using custom designed models automatically generated from CT data. Int J Radiat Oncol Biol Phys. 1996;35:383–97.

15. ICRU Report 46. Photon, electron, proton, and neutron interaction data for body tissues. Bethesda: International Commission on Radiation Units and Measurements; 1992.
16. Yu HT, Liu YW, Lin TY, Wang LW. BNCT treatment planning of recurrent head-and-neck cancer using THORplan. Appl Radiat Isot. 2011;69:1907–10.
17. Chadha M, Capala J, Coderre JA, Elowitz EH, Iwai J, Joel DD, Liu HB, Wielopolski L, Chanana AD. Boron neutron-capture therapy (BNCT) for glioblastoma multiforme (GBM) using the epithermal neutron beam at the Brookhaven National Laboratory. Int J Radiat Oncol Biol Phys. 1998;40:829–34.
18. Rasouli FS, Masoudi SF. A study on the optimum fast neutron flux for boron neutron capture therapy of deep-seated tumors. Appl Radiat Isot. 2015;96:45–51.